Frontolysis by surface heat flux in the eastern Japan Sea: Importance of mixed layer depth

Shun Ohishi[1], Hidenori Aiki[1,4], Tomoki Tozuka[2,4], and Meghan F. Cronin[3]

[1]Institute for Space-Earth Environmental Research, Nagoya University, Nagoya, Japan

[2]Department of Earth and Planetary Science, Graduate School of Science, The University of Tokyo, Tokyo, Japan

[3]NOAA Pacific Marine Environmental Laboratory, Seattle, Washington, USA

[4]Application Laboratory, Japan Agency for Marine-Earth Science and Technology, Yokohama, Japan

Journal of Oceanography (Revised)

Nov. 15, 2018

Corresponding author address: Shun Ohishi, Institute for Space-Earth Environmental Research, Nagoya University, Furo-cho, Chikusa-ku, Nagoya, Aichi, 464-8601, Japan. E-mail: ohishi@isee.nagoya-u.ac.jp, TEL: +81-52-789-3446, FAX: +81-52-788-6206

Abstract (249/250 words)

Frontolysis mechanisms by which surface heat flux relaxes the sea surface temperature (SST) front in the eastern Japan Sea (JS) are investigated in detail using observational datasets. On the warm southern side of the front, larger air-sea specific humidity and temperature differences induce stronger turbulent heat release compared to the cool northern side. As a result, stronger wintertime cooling and weaker summertime warming occur south of the front, and the meridional gradient in the surface net heat flux (NHF) tends to relax the SST front throughout the year. In the mixed-layer deepening phase (September–January), larger entrainment velocity occurs on the warm southern side because of weaker stratification. Since the resulting thicker mixed layer on the southern side is less sensitive to surface cooling, the mixed layer depth (MLD) gradient damps the frontolysis by the NHF gradient. In the shoaling phase (April–June), a deeper mixed layer south of the front is caused by the weaker warming and less sensitivity of the thicker mixed layer to shoaling effect by shortwave radiation. Owing to weaker sensitivity of the thicker mixed layer on the southern side to surface warming, the MLD gradient enhances the frontolysis by the NHF gradient. Therefore, it is shown that the mixed layer processes cause seasonality of weaker (stronger) frontolysis by surface heat fluxes damping (enhancing) the frontolysis by the NHF gradient in winter (summer). This study reveals unique features of the frontolysis in the eastern JS compared with the Agulhas Return Current and Kuroshio Extension regions.

Keywords (5-10 keywords)

frontolysis; mixed layer processes; entrainment; Japan Sea; sea surface temperature

front

1. Introduction

Mid-latitude climate system is strongly influenced by sea surface temperature (SST) fronts in western boundary current regions through their effects on the atmospheric static stability and pressure field (e.g. Nonaka and Xie 2003; Minobe et al. 2008; Takatama et al. 2012, 2015). Recent studies have demonstrated that both intensity and position of storm track activity are maintained to some extent by SST fronts using aqua planet experiments (e.g., Nakamura et al. 2008; Ogawa et al. 2012). In mid-latitude regions, the atmosphere also affects the oceanic field through several processes, such as surface heat flux (Cayan 1992), entrainment at the base of a mixed layer (Miller et al. 1994), and Ekman transport (Yasuda and Hanawa 1997).

One way to understand the air-sea interaction in western boundary current regions is to focus on reinforcement/relaxation processes of SST fronts, i.e. frontogenesis/frontolysis. As shown by Tozuka et al. (2018), the mixed layer depth (MLD) can play an important role in determining whether surface heat fluxes act to strengthen or degrade the horizontal gradient in mixed layer temperatures (MLTs) and the strength of the processes (Throughout this paper, the gradient indicates the meridional gradient, unless otherwise specified). In the Agulhas Return Current (ARC) region in the southwestern Indian Ocean, where a single strong SST front can be detected throughout the year and monsoon effects are small, frontogenesis is caused by a meridional cross-isotherm confluence with the southward warm and northward cool water advection toward the front on the northern and southern side of the front, respectively (Ohishi et al. 2017). It approximately balances with frontolysis by surface net heat flux (NHF), and thus the SST front is maintained.

Tozuka and Cronin (2014) and Ohishi et al. (2016) revealed the importance of mixed layer processes for the frontolysis, which enhance and damp frontolysis by the NHF gradient in austral summer and winter, respectively. In contrast to the ARC region, surface heat flux effect strengthens the SST front in the Kuroshio Extension (KE) region in boreal winter, because weak frontolysis by the small NHF gradient is overwhelmed by frontogenesis associated with the MLD gradient, which is caused by weaker stratification on the southern side of the front (Konda et al. 2010; Tozuka et al. 2017).

The Japan Sea (JS) is a marginal sea in the western North Pacific constituting the Kuroshio Current system and has interesting features such as a subpolar front located in its center (Park et al. 2004, 2007), inflow of warm water through the Tsushima Strait into the southern part of the front, a cyclonic gyre over the northern part (e.g. Isobe and Isoda 1997; Takikawa et al. 2005; Yoon and Kim 2009), and dry and cold winter monsoon winds blowing from Siberia (Kawamura and Wu 1998; Dorman et al. 2004). Characteristics of the SST front have been investigated using satellite observations (Park et al. 2004, 2007), and its impact on the atmosphere are also demonstrated by sensitivity experiments using atmospheric general circulation models (Chen et al. 2001; Yamamoto and Hirose 2007). However, detailed mechanisms of frontogenesis/frontolysis in the JS have not been fully investigated in previous studies. In this regard, Zhao et al. (2014) examined frontogenesis/frontolysis in the JS using an oceanic reanalysis dataset, but the distribution and amplitude of the MLD in an ocean reanalysis data are quite different from observations (Fig. 1; Fig. 9 of Lim et al. 2012). Also, other ocean reanalysis datasets have substantial biases in MLD, as reported by Toyoda et al. (2017). Even if ocean models have a high horizontal resolution, MLD biases can be formed (Ohishi et al. 2016, 2017), and this may lead to those in ocean reanalysis datasets. These MLD biases, which may result from deficiency in vertical mixing parameterization (Huang et al. 2014; Ohishi et al. 2016), are a serious problem, because they have substantial contributions to frontogenesis/frontolysis (Ohishi et al. 2016). As a result, mixed layer processes in frontogenesis/frontolysis in the JS remain unclear.

The objectives of this study are to quantitatively investigate frontogenesis/frontolysis in the JS based on the analysis scheme developed by Ohishi et al. (2016, 2017) using observational datasets with a special focus on mixed layer processes and to discuss differences with the ARC and KE regions. This paper is organized as follows. Observational datasets used in this study are described in Section 2. Section 3 discusses characteristics of SST fronts, frontogenesis/frontolysis, and causes of the NHF and MLD gradients. Conclusions are given in the final section.

2. Observational and reanalysis data

Monthly temperature/salinity climatology is obtained from the optimal interpolated Monthly Isopycnal/Mixed-layer Ocean Climatology (MIMOC; Schmidtko et al. 2013) on 0.5° longitude × 0.5° latitude grid with 81 layers. MIMOC is constructed mainly based on the Argo float profiles in 2007–2011 and by applying weighting and covariance functions that maintain the sharpness of fronts, making it suitable for frontal studies. We note that qualitatively the same results may be obtained even if we use temperature/salinity data prepared at the Scripps Institution of Oceanography (Roemmich and Gilson 2009) with a horizontal resolution of 1° and 58 vertical levels. We also use ship observational data from

Japan Oceanographic Data Center (JODC; http://www.jodc.go.jp/jodcweb/index.html) to confirm the MLD spatial pattern of the MIMOC. In this study, the MLD is defined as a depth at which the density is 0.125 kg m^{-3} larger than surface density and detected using the spline interpolation method of Akima (1970) at 0.1 m intervals. MLTs are the vertically-averaged temperatures within the mixed layer and estimated from the integrated spline function of Akima (1970). To estimate the number of the Argo float profiles, we regrid Advanced Quality Control (AQC) Argo Data version 1.2 (http://www.jamstec.go.jp/ARGO/argo_web/argo/?page_id=100&lang=en) produced by Japan Agency for Marine-Earth Science and Technology (JAMSTEC) to 0.5° longitude × 0.5° latitude grid. We use monthly-mean SSTs from Multi-scale Ultra-high Resolution Sea Surface Temperature (MURSST; https://mur.jpl.nasa.gov/) converted to 0.1° longitude × 0.1° latitude grid from 0.01° longitude × 0.01° latitude original grid for investigating characteristics of SST fronts in the JS. To examine the detail of surface heat fluxes, we use latent and sensible heat flux, longwave and shortwave radiation, wind speed, air specific humidity, and air temperatures at 10 m, surface saturated specific humidity, and SSTs from Japanese Ocean Flux Data Sets with Use of Remote Sensing Observations version 3 (J-OFURO3; Tomita et al. in press) with a horizontal resolution of 0.25°. At present, J-OFURO3 has the highest horizontal resolution among observational datasets including all variables associated with surface heat fluxes during the study period and represents fine spatial patterns of turbulent heat fluxes (figure not shown). We note that qualitatively the same results can be obtained even if Objectively Analyzed air-sea Fluxes (OAFlux; Yu and Weller 2007) with a horizontal resolution of 1° is used. Sea surface height is adopted from Archiving, Validation and Interpretation of Satellite Oceanographic data (AVISO; Ducet et al. 2000) on 0.25° longitude × 0.25° latitude grid. Ocean reanalysis data is also obtained from Japan Coastal Ocean Predictability Experiment 2 (JCOPE2) with a horizontal resolution of 1/12° and 46 vertical levels. The analysis period is from January 2007 to December 2011 to be consistent with the MIMOC.

3. Frontogenesis/Frontolysis in the Japan Sea

3.1 Frontogenesis/Frontolysis

In this study, the intensity and position of the SST front are defined as a maximum of the horizontal SST gradient at each longitude in 38°–42°N and its latitude, respectively. As reported by Park et al. (2004, 2007), in the eastern side of the JS, a single, strong, and relatively stable SST front is located along 40°N throughout the year (Figs. 2, 3), although the intensity is weak in summer (Figs. 3e, g). In the western side, two strong SST fronts with northwest-southeast and southwest-northeast orientations are distributed in the northern and southern parts in winter, respectively, but almost disappear in summer (Fig. 3). This leads to larger variations in the frontal position in the western side compared to the eastern side. As shown in Fig. 4, the number of Argo float observations in 2007–2011 is relatively large on both sides of the front in the eastern JS: its total within 3° north and south of the SST front in 135°–138°E is about 40 and 70 at each month throughout the year, respectively. In this study, we focus on the strong and stable SST front in the eastern portion of the JS between 135°E and 138°E, which is well resolved by the MIMOC product, since the relatively large number of Argo float observations have been deployed in this part of the JS.

As shown in Fig. 5, the intensity of the SST front in this region estimated from MURSST undergoes a seasonal variation with a maximum of 7.8 °C/100km in February and a minimum of 2.8 °C/100km in August. To investigate the frontogenesis/frontolysis quantitatively, we use the frontogenesis rate equation (e.g. Tozuka and Cronin 2014; Ohishi et al. 2016):

$$\frac{\partial}{\partial t}\left(-\frac{\partial T_{mix}}{\partial y}\right) = -\frac{\partial}{\partial y}\left(\frac{Q_{net} - q_{sw}(-H)}{\rho_0 c_p H}\right) - \frac{\partial}{\partial y}(oceanic\ term), \quad (1)$$

which is derived from the meridional derivative of the MLT T_{mix} balance equation (e.g. Moisan and Niiler 1998). We note that Eq. (1) is multiplied by –1 to specify that positive and negative values mean frontogenesis and frontolysis, respectively. Here, Q_{net} is NHF (positive values indicating the heat gain by the ocean from the atmosphere) and $q_{sw}(z)$ is downward shortwave radiation at depth z parameterized by

$$q_{sw}(z) = Q_{sw}\left\{Rexp\left(\frac{z}{\gamma_1}\right) + (1-R)exp\left(\frac{z}{\gamma_2}\right)\right\} \quad (2)$$

(Paulson and Simpson 1977), where Q_{sw} is surface net shortwave radiation, R $(= 0.58)$ is a separation constant, and $\gamma_1\ (= 0.35\ m)$ and $\gamma_2\ (= 23\ m)$ are attenuation length scales and set to the Type I (clear water) case from Jerlov (1976). Also, H is the MLD, $\rho_0 (= 1026\ kg\ m^{-3})$ is the density of the sea water, c_p $(= 3990\ J\ kg^{-1}\ °\mathrm{C}^{-1})$ is the specific heat of the sea water, and $(oceanic\ term)$

includes contributions from horizontal advection, entrainment, diffusion, and residual terms. In this study, the meridional derivative is calculated as the meridional difference between monthly climatologies averaged within the boxes 3° north and south of the monthly climatological front in 135°–138°E. We have confirmed that the results are qualitatively unchanged if the zonal/meridional width and zonal position of the boxes are changed by 1–2° of longitude or latitude. Figure 6 shows that the frontogenesis rate [the left-hand side (LHS) term of Eq. (1)] monthly climatology calculated from MIMOC is primarily associated with an annual harmonic, except for in May, because the intensity of the SST front estimated from MIMOC has a secondary maximum in June (figure not shown). The 1st term on the right-hand side (RHS) of Eq. (1), described as the NHF/MLD gradient in this study, has the dominant contribution to frontolysis throughout the year, while the oceanic term gradient [the 2nd term on the RHS of Eq. (1)], estimated as the difference between the frontogenesis rate and NHF/MLD gradient term, strengthens the SST front in almost all months. Although horizontal advection estimated from surface geostrophic velocity and MLTs contributes to frontogenesis in almost all months, it is smaller than the oceanic term gradient, and their seasonality does not correspond well (figure not shown).

3.2 Frontolysis by surface heat flux

To investigate the detailed mechanisms of the frontolysis by the surface heat flux, we decompose the NHF/MLD gradient term as

$$-\frac{\partial}{\partial y}\left(\frac{Q_{net} - q_{sw}(-H)}{\rho_0 c_p H}\right) = -\frac{1}{\rho_0 c_p H}\frac{\partial}{\partial y}\left(Q_{net} - q_{sw}(-H)\right) + \frac{Q_{net} - q_{sw}(-H)}{\rho_0 c_p H^2}\frac{\partial H}{\partial y}. \tag{3}$$

The NHF gradient term [the 1st term on the RHS of Eq. (3)] contributes to frontolysis throughout the year (Fig. 7), because of stronger cooling in winter and weaker warming in summer on the warm southern side of the front than the cool northern side (Fig. 8). On the other hand, the MLD gradient term [the 2nd term on the RHS of Eq. (3)] has different roles in frontogenesis/frontolysis depending upon season. In particular, the mixed layer south of the front is deeper than north of the front throughout the year, although the differences are not larger than the vertical resolution of the observational dataset in summer (Figs. 1, 9). This deeper mixed layer on the southern side than the northern side is confirmed by the ship observation data derived from JODC (figure not shown). The thicker mixed layer on the southern side is less sensitive to surface cooling in winter and heating in summer compared to the thinner mixed layer on the northern side. Therefore, the MLD gradient contributes to frontogenesis in winter and frontolysis in summer.

As shown in Fig. 7, the NHF gradient term has the dominant contribution to frontolysis by the NHF/MLD gradient in all months except for July. This is also confirmed using the metric proposed by Tozuka et al. (2018) that evaluates the relative importance of the NHF and MLD gradients (figure not shown). On the other hand, the NHF and MLD gradient terms have correlation values of −0.19 and 0.65 and regression values of −0.29 and 1.29 with the NHF/MLD gradient term, respectively. Therefore, frontolysis and frontogenesis by the MLD gradient term results in the seasonality, with stronger and weaker frontolysis by the NHF/MLD gradient in spring–summer and autumn–winter, respectively. As is clear from the above, both NHF and MLD gradients play important roles in the frontogenesis/frontolysis. Causes of the NHF and MLD gradients are described in subsections 3.2.1 and 3.2.2/3.2.3, respectively.

3.2.1 Cause of the NHF gradient

The NHF gradient can be decomposed as

$$-\frac{\partial Q_{net}}{\partial y} = -\frac{\partial Q_{lh}}{\partial y} - \frac{\partial Q_{sh}}{\partial y} - \frac{\partial Q_{lw}}{\partial y} - \frac{\partial Q_{sw}}{\partial y}, \tag{4}$$

where Q_{lh}, Q_{sh}, and Q_{lw} is latent heat flux, sensible heat flux, and net longwave radiation at the sea surface, respectively. The NHF gradient [the LHS term of Eq. (4)] is mainly caused by the latent heat flux gradient [the 1st term on the RHS of Eq. (4)] and partly by the sensible heat flux gradient [the 2nd term on the RHS of Eq. (4)] (Fig. 10), while the longwave and shortwave radiation gradients [the 3rd and 4th terms on the RHS of Eq. (4), respectively] have minor contributions. However, the shortwave radiation may have uncertainty because of the lack of the effect from low-level clouds on the warmer side of SST fronts, which reduce downward shortwave radiation reaching the sea surface as reported by recent ship observations in the KE region (Kawai et al. 2015).

The latent and sensible heat flux gradients can be further decomposed as

$$-\frac{\partial Q_{lh}}{\partial y} \equiv -\frac{\partial}{\partial y}\{C_{lh}u_{10}(q_s - q_a)\}$$

$$= -u_{10}(q_s - q_a)\frac{\partial C_{lh}}{\partial y} - C_{lh}(q_s - q_a)\frac{\partial u_{10}}{\partial y} \quad (5)$$

$$-C_{lh}u_{10}\frac{\partial q_s}{\partial y} + C_{lh}u_{10}\frac{\partial q_a}{\partial y} - (res)$$

and

$$-\frac{\partial Q_{sh}}{\partial y} \equiv -\frac{\partial}{\partial y}\{C_{sh}u_{10}(T_s - T_a)\}$$

$$= -u_{10}(T_s - T_a)\frac{\partial C_{sh}}{\partial y} - C_{sh}(T_s - T_a)\frac{\partial u_{10}}{\partial y} \quad (6)$$

$$-C_{sh}u_{10}\frac{\partial T_s}{\partial y} + C_{sh}u_{10}\frac{\partial T_a}{\partial y} - (res),$$

respectively. Here, $C_{lh} = \rho_a C_e L$, where ρ_a $(= 1.3\ kg\ m^{-3})$ is the air density, C_e is the transfer coefficient for latent heat, and L is the latent heat of evaporation, u_{10} is the wind speed at 10 m, q_s is surface saturated specific humidity, and q_a is surface air specific humidity. Also, $C_{sh} = \rho_a c_p C_h$, where C_h is the transfer coefficient for sensible heat, T_s is SSTs, and T_a is surface air temperatures. In this study, C_{lh} and C_{sh} are estimated by dividing Q_{lh} by $u_{10}(q_s - q_a)$ and Q_{sh} by $u_{10}(T_s - T_a)$ using daily data, respectively. (res) in Eqs. (5) and (6) denote the residual terms, which include sub-monthly terms. Figure 11 shows that the latent heat coefficient gradient, wind speed gradient, and the residual terms [the 1st, 2nd, and last terms on the RHS of Eq. (5), respectively] play minor roles in the formation of the latent heat flux gradient [the LHS term of Eq. (5)]. The surface saturated specific humidity gradient is larger than the air specific humidity gradient, and the surface saturated specific humidity gradient term [the 3rd term on the RHS of Eq. (5)] is dominant for the latent heat flux gradient. Since surface saturated specific humidity is almost determined by SSTs, the SST gradient induces the latent heat flux gradient through the formation of the surface saturated specific humidity gradient. As is clear from Fig. 12, the SST gradient term [the 3rd term on the RHS of Eq. (6)] is larger than the air temperature gradient term [the 4th term on the RHS of Eq. (6)], and the other terms have minor effects. Therefore, the SST gradient also causes the sensible heat flux gradient.

3.2.2 Cause of the MLD gradient in mixed-layer deepening phase

In the deepening phase of a mixed layer, a diagnostic equation for the entrainment velocity w_e:

$$\frac{1}{2}\alpha g H \Delta T w_e = m_0 u_*^3 + \frac{\alpha g}{\rho_0 c_p}\int_{-H}^{0} q_{sw}(z)dz - \frac{\alpha g H}{2\rho_0 c_p}\left(Q_{net} - q_{sw}(-H)\right) - m_c \frac{\alpha g H}{4\rho_0 c_p}\left(|Q_{net}| - Q_{net}\right) \quad (7)$$

(e.g. Niiler and Kraus 1977; Qiu and Kelly 1993) may be useful, where $\alpha\,(= 2.5 \times 10^{-4}\,°\mathrm{C}^{-1})$ is the thermal expansion coefficient, $g\,(= 9.8\,m\,s^{-2})$ is the acceleration of gravity, and $\Delta T (\equiv T_{mix} - T_{-H-20m})$ is the temperature difference between the mixed layer and entrained water. In this study, temperature 20m below the base of the mixed layer is used as the entrained water temperature following Ohishi et al. (2016, 2017). Even when the different definitions of the temperature difference (i.e. $\Delta T = T_{mix} - T_{-H}$ and $\Delta T = T_s - T_{-H-20m}$) are used, the results are qualitatively the same. m_0 $(= 0.5)$ is the coefficient for the efficiency of wind stirring, $u_*(= u_{10}\sqrt{\rho_a C_D/\rho_0})$ is the frictional velocity, where C_D $(= 1.5 \times 10^{-3})$ is the drag coefficient, and m_c $(= 0.83)$ is the convective efficiency coefficient. Figure 10 indicates that the tendency of the observed MLD gradient equivalent to the observed entrainment velocity gradient has negative values in September–January when the MLD deepens on both sides of the front. This means that the observed mixed layer on the southern side deepens more rapidly compared with the northern side. Although the diagnostic entrainment velocity north and south of the front is about two and three–four times larger compared with the observed MLD tendency, respectively (figure not shown), its gradient also shows negative values in the deepening phase (Fig. 13).

Although the diagnostic entrainment velocity equation [Eq. (7)] represents an energy balance between wind stirring, heat fluxes, and entrained water, horizontal advection and divergence/convergence caused by ageostrophic currents may also have influences. Since the geostrophic horizontal advection contributes to frontogenesis (figure not shown) and warmer water is advected on the southern side of the front compared to the northern side, the opposite MLD gradient to the observation would be formed if the horizontal advection were the dominant cause for the formation of the entrainment velocity. While effects of geostrophic shear have substantial contributions to ageostrophic currents (Cronin and Tozuka 2016), these terms cannot be accurately estimated from the available observations, and consequently their estimation is beyond the scope of this study. Therefore, because the diagnostic entrainment velocity gradient has the same characteristics as the observation, the diagnostic entrainment velocity equation [Eq. (7)] is used for investigating the cause of the MLD gradient around the SST front.

The diagnostic entrainment velocity gradient is decomposed as

$$
\begin{aligned}
\frac{\partial w_e}{\partial y} \equiv \frac{\partial}{\partial y}\left(\frac{u + \int q dz + HQ + Hq}{H\Delta T}\right) \\
= \frac{1}{H\Delta T}\frac{\partial u}{\partial y} + \frac{1}{H\Delta T}\frac{\partial \int q dz}{\partial y} + \frac{1}{\Delta T}\frac{\partial Q}{\partial y} + \frac{1}{\Delta T}\frac{\partial q}{\partial y} \\
- \frac{u + \int q dz}{H^2 \Delta T}\frac{\partial H}{\partial y} - \frac{u + \int q dz + HQ + Hq}{H^2 \Delta T}\frac{\partial \Delta T}{\partial y}.
\end{aligned}
\tag{8}
$$

Here, each term on the RHS indicates contributions from the gradients of the wind speed, incidence of shortwave radiation, NHF, downward shortwave radiation at the base of a mixed layer, MLD, and stratification to the diagnostic entrainment velocity gradient. Figure 14 shows contribution ratios of each term on the RHS of Eq. (8) to the diagnostic entrainment velocity gradient [the LHS term of Eq. (8)]. The contribution from the stratification gradient is dominant for the diagnostic entrainment velocity gradient, while the other terms have minor roles. As shown in Fig. 15, the temperature difference in the southern region is smaller than the northern region. Since a smaller (larger) amount of energy is needed for entrainment when vertical stratification is weaker (stronger), larger (smaller) entrainment velocity occurs south (north) of the front. As shown in previous studies, circulation in the JS can be broadly broken into two parts: the southern side of the front with the water originating from the Kuroshio Current through the Tsushima Strait and the northern side with the large cyclonic gyre (Isobe and Isoda 1997; Takikawa et al. 2005; Yoon and Kim 2009). This difference of water mass origin may be the cause of the stratification gradient. Interestingly, the NHF gradient in the eastern JS has a minor contribution to the formation of the entrainment velocity gradient, even though it is about two times larger in the eastern JS than in the ARC region (see Fig. 10 in Ohishi et al. 2016), where the main cause is the NHF gradient. Instead, the wintertime formation processes of the MLD gradient in the eastern JS are similar to the KE region with the large vertical stratification gradient and small NHF gradient caused by the combination of the weather conditions with northerly and northwesterly wind (Konda et al. 2010; Tozuka et al. 2017).

3.2.3 Cause of the MLD gradient in mixed-layer shallowing phase

On the assumption that the diagnostic entrainment velocity may be set to zero in shoaling phase, we can obtain the Monin-Obukhov Depth (MOD) H_m:

$$H_m = \frac{\frac{2\rho_0 c_p m_0}{\alpha g} u_*^3 + 2\int_{-H_m}^{0} q_{sw}(z)dz}{Q_{net} + q_{sw}(-H_m)} \qquad (9)$$

(e.g. Niiler and Kraus 1977; Qiu and Kelly 1993). In April–June when the MLD becomes shallow on both sides of the front, the MOD reproduces the deeper and shallower observed MLD on the southern and northern regions, respectively, although the amplitude of the MOD differs from the MLD (Fig. 16). Therefore, the MOD can be used to examine the cause of the MLD gradient in April–June.

The MOD gradient is represented as

$$
\begin{aligned}
\frac{\partial H_m}{\partial y} &\equiv \frac{\partial}{\partial y}\left(\frac{u+\int q dz}{Q_{net}+q_{sw}(-H_m)}\right) \\
&= \frac{1}{Q_{net}+q_{sw}(-H_m)}\frac{\partial u}{\partial y} + \frac{1}{Q_{net}+q_{sw}(-H_m)}\frac{\partial \int q dz}{\partial y} \\
&\quad - \frac{u+\int q dz}{\left(Q_{net}+q_{sw}(-H_m)\right)^2}\frac{\partial Q_{net}}{\partial y} - \frac{u+\int q dz}{\left(Q_{net}+q_{sw}(-H_m)\right)^2}\frac{\partial q_{sw}(-H_m)}{\partial y}.
\end{aligned}
\tag{10}
$$

Here, each term on the RHS denotes contributions from respectively the gradients of the wind speed, incidence of shortwave radiation, NHF, and shortwave radiation at the base of the MOD. Figure 17 shows contribution ratios of each term on the RHS of Eq. (10) to the MOD gradient [the LHS term of Eq. (10)]. The MOD gradient is dominated mainly by the NHF gradient term [the 3rd term on the RHS of Eq. (10)] and partly by the shortwave radiation incidence term [the 2nd term on the RHS of Eq. (10)] in April, and mainly by the latter and partly by the former in May–June, while the other terms have small contributions. Strong heating by shortwave radiation occurs in the shoaling phase, but it is counteracted by larger turbulent heat release south of the front than north of the front (Fig. 10). The resulting weaker surface net heating on the southern side leads to weaker shoaling and thus deeper mixed layer compared with the northern side.

The shortwave radiation incidence gradient is decomposed as

$$
\begin{aligned}
&\frac{\partial}{\partial y}\int_{-H_m}^{0} q(z)dz \\
&= \left[\gamma_1 R\left\{1-exp\left(-\frac{H_m}{\gamma_1}\right)\right\}+\gamma_2(1-R)\left\{1-exp\left(-\frac{H_m}{\gamma_2}\right)\right\}\right]\frac{\partial Q_{sw}}{\partial y} \\
&+Q_{sw}\left[R\left\{1-exp\left(-\frac{H_m}{\gamma_1}\right)\right\}+(1-R)\left\{1-exp\left(-\frac{H_m}{\gamma_2}\right)\right\}\right]\frac{\partial H_m}{\partial y}.
\end{aligned}
\tag{11}
$$

While the shortwave radiation gradient term [the 1st term on the RHS of Eq. (11)] shows minor effect, the MOD gradient term [the 2nd term on the RHS of Eq. (11)] plays a major role in the shortwave radiation incidence gradient [the LHS term of Eq. (11)] in April–June (Fig. 18). Owing to the deeper MLD in the southern region, the shortwave radiation incidence is larger than the northern region. The shortwave radiation incidence in the MOD [Eq. (9)] represents sensitivity of the MOD to stratification effect by shortwave radiation. Therefore, the thicker (thinner) mixed layer south (north) of the front is less (more) sensitive to the stratification effect and is favorable for maintenance of the deeper (shallower) mixed layer. This formation mechanism in the eastern JS is different from that in the ARC region, where only the NHF gradient forms the MLD gradient (Ohishi et al. 2016).

4. Conclusions

We have performed a detailed investigation of the frontolysis mechanisms in the eastern JS using observational dataset. In the western side of the JS, two SST fronts with northwest-southeast and southwest-northeast directions in the northern and southern parts can be detected in winter, respectively, but both fronts disappear in summer. In the eastern side, a single strong SST front is located along 40°N, and it shows relatively stable meridional position and undergoes the seasonal variation with stronger intensity in winter than summer.

The SST front in the eastern side is predominantly relaxed by the NHF throughout the year and strengthened by the oceanic term gradient estimated as residual in almost all months. Figure 19 is schematic diagrams of the frontolysis by the surface heat flux. On the southern side of the front, latent heat release is larger than the northern side, because the SST front induces the larger surface saturated specific humidity gradient compared with the air specific humidity gradient. The sensible heat flux gradient is formed in a similar way. Therefore, turbulent heat release south of the front is larger than north of the front throughout the year. This leads to stronger (weaker) surface cooling in winter and weaker (stronger) surface warming in summer on the southern (northern) side of the front. Consequently, the NHF gradient relaxes the SST front throughout the year.

In the mixed-layer deepening phase (September–January), larger entrainment velocity occurs on the southern portion of the front because of weaker stratification, and thus a deeper mixed layer is formed. Since the thicker mixed layer south of the front is less sensitive to surface cooling compared to the thinner mixed layer north of the front, the MLD gradient contributes to frontogenesis and damps the frontolysis by the NHF gradient.

In the shallowing phase (April–June), the deeper mixed layer is formed in the southern region because of the weaker warming and less sensitivity of the thicker mixed layer to shoaling effect by shortwave radiation compared to the northern region. Since the resulting thicker mixed layer on the southern side is less sensitive to surface warming, the MLD gradient enhances the frontolysis by the NHF gradient. Therefore, frontolysis by surface heat fluxes is damped (enhanced) by mixed layer processes in autumn–winter (spring–summer).

This study reveals that the frontolysis mechanisms in the eastern JS are different from those in the ARC and KE regions. In winter, the NHF relaxes the SST front in the ARC region and eastern JS where frontolysis by the NHF gradient exceeds the frontogenesis by the MLD gradient. On the other hand, the NHF strengthens the SST front in the KE region. This occurs because the combination of weather conditions with northerly and northwesterly winds in the KE region causes the NHF gradient to be small and the large MLD gradient strengthens the SST front. Although the NHF gradient is larger in the eastern JS compared to the ARC region where the NHF gradient results in the MLD gradient through the formation of the entrainment velocity gradient, the main cause of the MLD gradient in the eastern JS is the stratification gradient, which is similar to the KE region. In summer, while the MLD gradient is caused by the NHF gradient in the ARC region as in austral winter, it is caused by the sensitivity difference of the MLD to shoaling effect by shortwave radiation as well as the NHF gradient in the eastern JS.

Although Qiu et al. (2014) pointed out substantial sub-monthly effects in the NHF/MLD gradient term [the 1st term on the RHS of Eq.(1)], they are not considered in this study. Also, observational errors are not included in this study. In addition, the oceanic term gradient [the 2nd term on the RHS of Eq. (1)] contributing to frontogenesis is estimated as the residual in the eastern side of the JS, and the frontogenesis/frontolysis remains unclear in the western side where the number of observations in the ocean interior is small north of the front. Further investigations of the frontogenesis/frontolysis might become possible, if observational datasets were improved to more accurately capture frontal features by expanding the data coverage in both the ocean interior and the frontal region, and/or ocean/coupled general circulation models and oceanic reanalysis systems were improved. For the latter, the development of vertical mixing schemes that enable us to reproduce the observed MLD (Furuichi et al. 2012; Watanabe and Hibiya 2013) and conserving each term of the heat budget equation at each timestep are necessary.

Previous studies quantitatively investigated frontogenesis/frontolysis by horizontal advection, surface heat fluxes, and entrainment in the ARC region (Ohishi et al. 2016, 2017) and frontogenesis by surface heat fluxes in the KE region (Tozuka et al. 2017). In this study, we have confirmed that the previous method can be applied to quantitatively investigate frontolysis by surface heat fluxes in the eastern JS. Investigations of frontogenesis/frontolysis using the previous and present methods in the frontal regions such as the tropical Atlantic and Pacific (e.g. Jochum et al. 2004; Willett et al. 2006), Gulf Stream (e.g. Kelly et al. 2010; Kwon et al. 2010), and Brazil-Malvinas Confluence regions (e.g. Saraceno et al. 2004; Tokinaga et al. 2005) could enable us to extend understanding of tropical and mid-latitude air-sea interaction. Also, with the accumulation of Argo float observations over the global ocean and development of satellite observations, salinity fronts have attracted much attention recently (Kao and Lagerloef 2015; Yu 2015). Recent studies pointed out their importance for the formation of the barrier layer and mode water (Cronin and McPhaden 2002; Katsura et al. 2015; Katsura 2018). Since the balance equation of salinity is similar to that of temperature, a similar quantitative analysis of sea surface salinity fronts may shed new light on the ocean interior structure studies.

Acknowledgments

We are very thankful to two anonymous reviewers for their constructive and useful comments. This study was supported by the Japan Society for Promotion of Science through Grant-in-Aid for Scientific Research on Innovative Areas (Grant Number JP16H01589). PMEL contribution 4761.

References

Akima H (1970) A new method of interpolation and smooth curve fitting based on local procedures. J Assoc Comput Mach 17:589–602. doi: 10.1145/321607.321609

Cayan DR (1992) Latent and sensible heat flux anomalies over the Northern Oceans: Driving the sea surface temperature. J Phys Oceanogr 22:859–881. doi: 10.1175/1520-0485(1992)022<0859:LASHFA>2.0.CO;2

Chen SS, Zhao W, Tenerelli JE, Evans RH, Halliwell V (2001) Impact of the AVHRR sea surface temperature on atmospheric forcing in the Japan/East Sea. Geophys Res Lett 28:4539–4542. doi: 10.1029/2001GL013511

Cronin MF, McPhaden MJ (2002) Barrier layer formation during westerly wind bursts. J Geophys Res Ocean 107:8020. doi: 10.1029/2001JC001171

Cronin MF, Tozuka T (2016) Steady state ocean response to wind forcing in extratropical frontal regions. Sci Rep 6:28842. doi: 10.1038/srep28842

Dorman CE, Beardsley RC, Dashko NA, Friehe CA, Kheilf D, Cho K, Limeburner R, Varlamov SM (2004) Winter marine atmospheric conditions over the Japan Sea. J Geophys Res 109:C12011. doi: 10.1029/2001JC001197

Ducet N, Le Traon PY, Reverdin G (2000) Global high-resolution mapping of ocean circulation from TOPEX/Poseidon and ERS-1 and -2. J Geophys Res 105:19477–19498. doi: 10.1029/2000JC900063

Furuichi N, Hibiya T, Niwa Y (2012) Assessment of turbulence closure models for resonant inertial response in the oceanic mixed layer using a large eddy simulation model. J Oceanogr 68:285–294. doi: 10.1007/s10872-011-0095-3

Huang CJ, Qiao F, Dai D (2014) Evaluating CMIP5 simulations of mixed layer depth during summer. J Geophys Res Ocean 119:2568–2582. doi: 10.1002/2013JC009535

Isobe A, Isoda Y (1997) Circulation in the Japan Basin, the northern part of the Japan Sea. J Oceanogr 53:373–381

Jerlov NG (1976) Marine Optics. Elsevier, Philadelphia, 231pp

Jochum M, Malanotte-Rizzoli P, Busalacchi A (2004) Tropical instability waves in the Atlantic Ocean. Ocean Model 7:145–163. doi: 10.1016/S1463-5003(03)00042-8

Kao HY, Lagerloef GSE (2015) Salinity fronts in the tropical Pacific Ocean. J Geophys Res Ocean 120:1096–1106. doi: 10.1002/ 2014JC010114

Katsura S (2018) Properties, formation, and dissipation of the North Pacific Eastern Subtropical Mode Water and its impact on interannual spiciness anomalies. Prog Oceanogr 162:120–131. doi: 10.1016/j.pocean.2018.02.023

Katsura S, Oka E, Sato K (2015) Formation mechanism of barrier layer in the subtropical Pacific. J Phys Oceanogr 45:2790–2805. doi: 10.1175/JPO-D-15-0028.1

Kawai Y, Miyama T, Iizuka S, Manda A, Yoshioka MK, Katagiri S, Tachibana Y, Nakamura H (2015) Marine atmospheric boundary layer and low-level cloud responses to the Kuroshio Extension front in the early summer of 2012: Three-vessel simultaneous observations and numerical simulations. J Oceanogr 71:511–526. doi: 10.1007/978-4-431-56053-1_3

Kawamura H, Wu P (1998) Formation mechanism of Japan Sea proper water in the flux center off Vladivostok. J Geophys Res 103:21611–21622. doi: 10.1029/98JC01948

Kelly KA, Small RJ, Samelson RM, Qiu B, Joyce TM, Kwon YO, Cronin MF (2010) Western boundary currents and frontal air-sea interaction: Gulf Stream and Kuroshio Extension. J Clim 23:5644–5667. doi: 10.1175/2010JCLI3346.1

Konda M, Ichikawa H, Tomita H, Cronin MF (2010) Surface heat flux variations across the Kuroshio Extension as observed by surface flux buoys. J Clim 23:5206–5221. doi: 10.1175/2010jcli3391.1

Kwon Y-O, Alexander MA, Bond NA, Frankignoul C, Nakamura H, Qiu B, Thompson LA (2010) Role of the Gulf Stream and Kuroshio–Oyashio systems in large-scale atmosphere–ocean interaction: A review. J Clim 23:3249–3281. doi: 10.1175/2010JCLI3343.1

Lim S, Jang CJ, Oh IS, Park J (2012) Climatology of the mixed layer depth in the East/Japan Sea. J Mar Syst 96–97:1–14. doi: 10.1016/j.jmarsys.2012.01.003

Miller AJ, Cayan DR, Barnett TP, Graham NE, Oberhuber JM (1994) Interdecadal variability of the Pacific Ocean: Model response to observed heat flux and wind stress anomalies. Clim Dyn 9:287–302. doi: 10.1007/BF00204744

Minobe S, Kuwano-Yoshida A, Komori N, Xie S-P, Small RJ (2008) Influence of the Gulf Stream on the troposphere. Nature 452:206–209. doi: 10.1038/nature06690

Miyazawa Y, Zhang R, Guo X, Tamura H, Ambe D, Lee JS, Okuno A, Yoshinari H, Setou T, Komatsu K (2009) Water mass variability in the western North Pacific detected in a 15-year eddy resolving ocean reanalysis. J Oceanogr 65:737–756. doi: 10.1007/s10872-009-0063-3

Moisan JR, Niiler PP (1998) The Seasonal heat nudget of the North Pacific: Net heat flux and heat storage rates (1950–1990). J Phys Oceanogr 28:401–421. doi:

10.1175/1520-0485(1998)028<0401:TSHBOT>2.0.CO;2

Nakamura H, Sampe T, Goto A, Ohfuchi W, Xie S-P (2008) On the importance of midlatitude oceanic frontal zones for the mean state and dominant variability in the tropospheric circulation. Geophys Res Lett 35:L15709. doi: 10.1029/2008GL034010

Niiler PP, Kraus EB (1977) One-dimensional models of the upper ocean. Pergamon New York 143–172

Nonaka M, Xie S-P (2003) Covariations of sea surface temperature and wind over the Kuroshio and its extension: Evidence for ocean-to-atmosphere feedback. J Clim 16:1404–1413. doi: 10.1175/1520-0442(2003)16<1404:COSSTA>2.0.CO;2

Ogawa F, Nakamura H, Nishii K, Miyasaka T, Kuwano-Yoshida A (2012) Dependence of the climatological axial latitudes of the tropospheric westerlies and storm tracks on the latitude of an extratropical oceanic front. Geophys Res Lett 39:L05804. doi: 10.1029/2011GL049922

Ohishi S, Tozuka T, Cronin MF (2017) Frontogenesis in the Agulhas Return Current region simulated by a high-resolution CGCM. J Phys Oceanogr 47:2691–2710. doi: 10.1175/JPO-D-17-0038.1

Ohishi S, Tozuka T, Komori N (2016) Frontolysis by surface heat flux in the Agulhas Return Current region with a focus on mixed layer processes: observation and a high-resolution CGCM. Clim Dyn 47:3993–4007. doi: 10.1007/s00382-016-3056-0

Park K-A, Chung J yul, Kim K (2004) Sea surface temperature fronts in the East (Japan) Sea and temporal variations. Geophys Res Lett 31:L07304. doi:

10.1029/2004GL019424

Park K-A, Ullman DS, Kim K, Yul Chung J, Kim K-R (2007) Spatial and temporal variability of satellite-observed subpolar front in the East/Japan Sea. Deep Res Part I 54:453–470. doi: 10.1016/j.dsr.2006.12.010

Paulson CA, Simpson JJ (1977) Irradiance measurements in the upper ocean. J Phys Oceanogr 7:952–956. doi: 10.1175/1520-0485(1977)007<0952:IMITUO>2.0.CO;2

Qiu B, Kelly KA (1993) Upper-ocean heat balance in the Kuroshio Extension region. J Phys Oceanogr 23:2027–2041. doi: 10.1175/1520-0485(1993)023<2027:UOHBIT>2.0.CO;2

Qiu C, Kawamura H, Mao H, Wu J (2014) Mechanisms of the disappearance of sea surface temperature fronts in the subtropical North Pacific Ocean. J Geophys Res Ocean 119:4389–4398. doi: 10.1002/2014JC010142

Roemmich D, Gilson J (2009) The 2004-2008 mean and annual cycle of temperature, salinity, and steric height in the global ocean from the Argo Program. Prog Oceanogr 82:81–100. doi: 10.1016/j.pocean.2009.03.004

Saraceno M, Provost C, Piola AR, Bava J, Gagliardini A (2004) Brazil Malvinas frontal system as seen from 9 years of advanced very high resolution radiometer data. J Geophys Res 109:C05027. doi: 10.1029/2003JC002127

Schmidtko S, Johnson GC, Lyman JM (2013) MIMOC: A global monthly isopycnal upper-ocean climatology with mixed layers. J Geophys Res Ocean 118:1658–1672. doi: 10.1002/jgrc.20122

Takatama K, Minobe S, Inatsu M, Small RJ (2012) Diagnostics for near-surface wind convergence/divergence response to the Gulf Stream in a regional atmospheric model. Atmos Sci Lett 13:16–21. doi: 10.1002/asl.355

Takatama K, Minobe S, Inatsu M, Small RJ (2015) Diagnostics for near-surface wind response to the Gulf Stream in a regional atmospheric model. J Clim 28:238–255. doi: 10.1175/JCLI-D-13-00668.1

Takikawa T, Yoon J-H, Cho K-D (2005) The Tsushima Warm Current through Tsushima Straits estimated from ferryboat ADCP data. J Phys Oceanogr 35:1154–1168. doi: 10.1175/JPO2742.1

Tokinaga H, Tanimoto Y, Xie SP (2005) SST-induced surface wind variations over the Brazil-Malvinas Confluence: Satellite and in situ observations. J Clim 18:3470–3482. doi: 10.1175/JCLI3485.1

Tomita H, Hihara T, Kako S, Kubota M, Kutsuwada K An introduction to J-OFURO3, a third-generation Japanese ocean flux data set using remote-sensing observations. J Oceanogr. doi: 10.1007/s10872-018-0493-x

Toyoda T, Fujii Y, Kuragano T, Kamachi M, Ishikawa Y, Masuda S, Sato K, Awaji T, Hernandez F, Ferry N, Guinehut S, Martin MJ, Peterson KA, Good SA, Valdivieso M, Haines K, Storto A, Masina S, Köhl A, Zuo H, Balmaseda M, Yin Y, Shi L, Alves O, Smith G, Chang YS, Vernieres G, Wang X, Forget G, Heimbach P, Wang O, Fukumori I, Lee T (2017) Intercomparison and validation of the mixed layer depth fields of global ocean syntheses. Clim Dyn 49:753–773. doi: 10.1007/s00382-015-2637-7

Tozuka T, Cronin MF (2014) Role of mixed layer depth in surface frontogenesis: The Agulhas Return Current front. Geophys Res Lett 41:2447–2453. doi: 10.1002/2014GL059624

Tozuka T, Cronin MF, Tomita H (2017) Surface frontogenesis by surface heat fluxes in the upstream Kuroshio Extension region. Sci Rep 7:10258. doi: 10.1038/s41598-017-10268-3

Tozuka T, Ohishi S, Cronin MF (2018) A metric for surface heat flux effect on horizontal sea surface temperature gradients. Clim Dyn 51:547–561. doi: 10.1007/s00382-017-3940-2

Watanabe M, Hibiya T (2013) Assessment of mixed layer models embedded in an ocean general circulation model. J Oceanogr 69:329–338. doi: 10.1007/s10872-013-0176-6

Willett CS, Leben RR, Lavín MF (2006) Eddies and tropical instability waves in the eastern tropical Pacific: A review. Prog Oceanogr 69:218–238. doi: 10.1016/j.pocean.2006.03.010

Yamamoto M, Hirose N (2007) Impact of SST reanalyzed using OGCM on weather simulation: A case of a developing cyclone in the Japan Sea area. Geophys Res Lett 34:L05808. doi: 10.1029/2006GL028386

Yasuda T, Hanawa K (1997) Decadal changes in the mode waters in the midlatitude North Pacific. J Phys Oceanogr 27:858–870. doi: 10.1175/1520-0485(1997)027<0858:DCITMW>2.0.CO;2

Yoon JH, Kim YJ (2009) Review on the seasonal variation of the surface circulation in the Japan/East Sea. J Mar Syst 78:226–236. doi: 10.1016/j.jmarsys.2009.03.003

Yu L (2015) Sea-surface salinity fronts and associated salinity-minimum zones in the tropical ocean. J Geophys Res Ocean 120:4205–4225. doi: doi:10.1002/2015JC010790

Yu L, Weller RA (2007) Objectively analyzed air–sea heat fluxes for the global icefree oceans (1981–2005). Bull Am Meteorol Soc 88:527–539. doi: 10.1175/BAMS-88-4-527

Zhao N, Manda A, Han Z (2014) Frontogenesis and frontolysis of the subpolar front in the surface mixed layer of the Japan Sea. J Geophys Res Ocean 119:1498–1509. doi: 10.1002/2013JC009419

Figure caption:

Fig. 1 Monthly climatology of mixed layer depth (MLD) in (a) February, (c) May, (e) August, and (g) November derived from outputs of an ocean reanalysis system, Japan Coastal Ocean Predictability Experiment 2 (JCOPE 2; Miyazawa et al. 2009). (b), (d), (f), and (h) As in (a), (c), (e), and (g), respectively, but for derived from Monthly Isophycnal/Mixed-layer Ocean Climatology (MIMOC; Schmidtko et al. 2013). Note that the MLD is defined as the a depth at which the density is 0.125 kg m^{-3} larger than surface density in both datasets. Thin (Thick) contour intervals are 10 (40) m in 0–200 m in (a)–(b) and 5 (20) m in (c)–(h). In (b), (d), (f), and (h), black line indicates monthly climatology of the sea surface temperature (SST) front position.

Fig. 2 Annual mean of the (a) position and (b) intensity of the SST front. Error bars are standard deviations in the analysis period. In (a), color indicates the amplitude of the SST gradient and white contour denotes SST climatology. Thin (Thick) contour intervals are 0.5 (5) °C.

Fig. 3 As in Fig. 2, but for monthly mean in (a), (c) February, (b), (d) May, (e), (g) August, and (f), (h) November.

Fig. 4 The total number of observations by the Argo floats in 2007–2011. A black line shows the annual mean of the SST front position. An orange (A cyan) box denotes the 3° longitude × 3° latitude averaging area on the southern (northern) side of the SST front. Note that white color indicates less than 6 observations.

Fig. 5 Monthly-mean intensity of the SST front averaged within 135°–138°E, which is derived from MURSST.

Fig. 6 Monthly climatology of each term of Eq. (1): the frontogenesis rate [the left-hand side term (LHS); black bar] estimated from MIMOC, the surface net heat flux

(NHF)/MLD gradient term [the 1st term on the right-hand side (RHS); red line], and the oceanic term gradient (the 2nd term on the RHS; blue line).

Fig. 7 Monthly climatology of each term of Eq. (3): the NHF/MLD gradient term (the LHS term; black bar), the NHF gradient term (the 1st term on the RHS; red line), and the MLD gradient term (the 2nd term on the RHS; blue line).

Fig. 8 Monthly climatology of NHF in (a) February, (b) May, (c) August, and (d) November. Thin (Thick) counter intervals are 25 (100) W/m^2.

Fig. 9 Monthly climatology of the MLD on the southern (red line) and northern (blue line) sides of the front and the MLD gradient (black bar).

Fig. 10 Monthly climatology of each term of Eq. (4): the NHF gradient (the LHS term; black bar), the latent and sensible flux gradient terms (the 1st and 2nd terms on the RHS; red and blue lines), and the longwave and shortwave radiation gradient terms (the 3rd and 4th terms on the RHS; orange and cyan lines).

Fig. 11 Monthly climatology of each term of Eq. (5): the latent heat flux gradient (the LHS term), the latent heat coefficient gradient term (the 1st term on the RHS; yellow line), the wind speed gradient term (the 2nd term on the RHS; green line), the surface saturated specific humidity gradient term (the 3rd term on the RHS; blue line), the air specific humidity gradient term (the 4th term on the RHS; red line), and the residual term (the last term on the RHS; gray line).

Fig. 12 Monthly climatology of each term of Eq. (6): the sensible heat flux gradient (the LHS term; black bar), the sensible heat coefficient gradient term (the 1st term on the RHS; yellow line), the wind speed gradient term (the 2nd term on the RHS; green line), the SST gradient term (the 3rd term on the RHS; blue line), the air temperature gradient term (the 4th term on the RHS; red line), and the residual term (the last term on the RHS; gray line).

Fig. 13 Monthly climatology of the diagnostic entrainment velocity gradient (black bar), and the entrainment velocity on the southern (red line) and northern (blue line) sides in September–January when the observed MLD deepens on the both sides of the front.

Fig. 14 Monthly climatology of contribution ratios of each term on the RHS of Eq. (8) to the diagnostic entrainment velocity gradient [the LHS term of Eq. (8)]: the gradients of the wind speed (the 1st term; green), incidence of shortwave radiation (the 2nd term; blue), NHF (the 3rd term; red), downward shortwave radiation at the base of mixed layer (the 4th term; orange), MLD (the 5th term; gray), and stratification (the last term; cyan).

Fig. 15 Monthly climatology of the temperature difference between the mixed layer and entrained water in September–January. Black line denotes the monthly climatological SST front position. Thin (Thick) white contour intervals are 1 (5) °C.

Fig. 16 Monthly climatology of the Monin-Obukhov Depth (MOD; bar) and observed MLD (line) on the southern (red) and northern (blue) regions in April–June when the MLD becomes shallower on both sides of the front.

Fig. 17 Monthly climatology of contribution ratios from each term on the RHS of Eq. (10) to the MOD gradient [the LHS term of Eq. (10)]: the gradients of the wind speed (the 1st term; green), incidence of shortwave radiation (the 2nd term; blue), NHF (the 3rd term; red), and shortwave radiation at the base of the MOD (the 4th term; orange) in April–June.

Fig. 18 Monthly climatology of contribution ratios from the gradients of shortwave radiation [the 1st term on the RHS of Eq. (11); red] and MOD [the 2nd term on the

RHS of Eq. (11); blue] to the shortwave radiation incidence gradient [the LHS term of Eq. (11)] in April–June.

Fig. 19 Schematic diagrams of frontolysis by surface heat flux in the eastern Japan Sea during the (a) deepening and (b) shoaling phase.

Figures

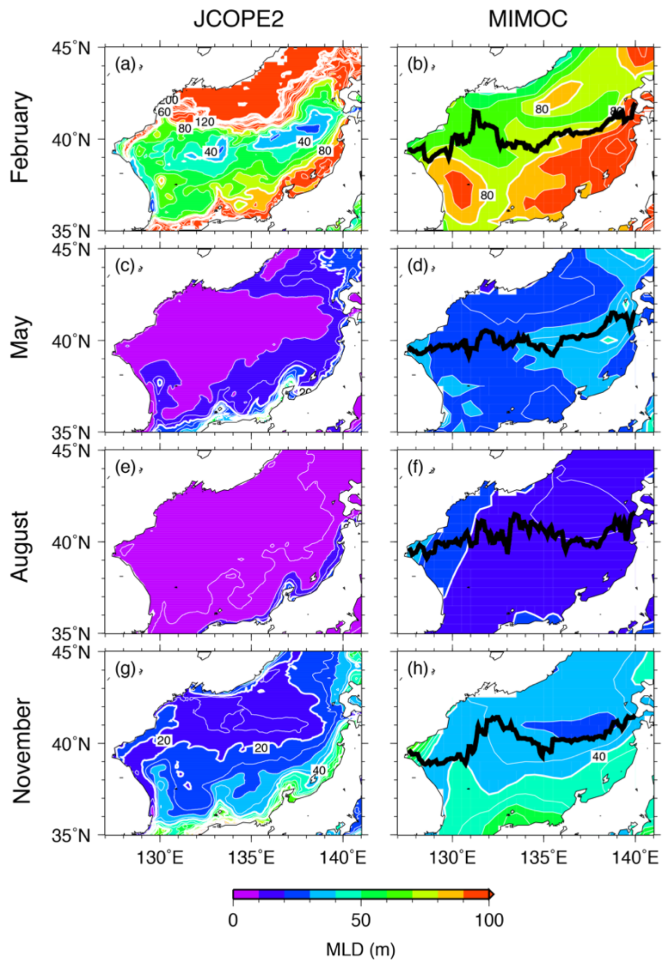

Fig. 1 Monthly climatology of mixed layer depth (MLD) in (a) February, (c) May, (e) August, and (g) November derived from outputs of an ocean reanalysis system, Japan Coastal Ocean Predictability Experiment 2 (JCOPE 2; Miyazawa et al. 2009). (b), (d), (f), and (h) As in (a), (c), (e), and (g), respectively, but for derived from Monthly Isophycnal/Mixed-layer Ocean Climatology (MIMOC; Schmidtko et al. 2013). Note that the MLD is defined as the a depth at which the density is 0.125 kg m^{-3} larger than surface density in both datasets. Thin (Thick) contour intervals are 10 (40) m in 0–200 m in (a)–(b) and 5 (20) m in (c)–(h). In (b), (d), (f), and (h), black line indicates monthly climatology of the sea surface temperature (SST) front position.

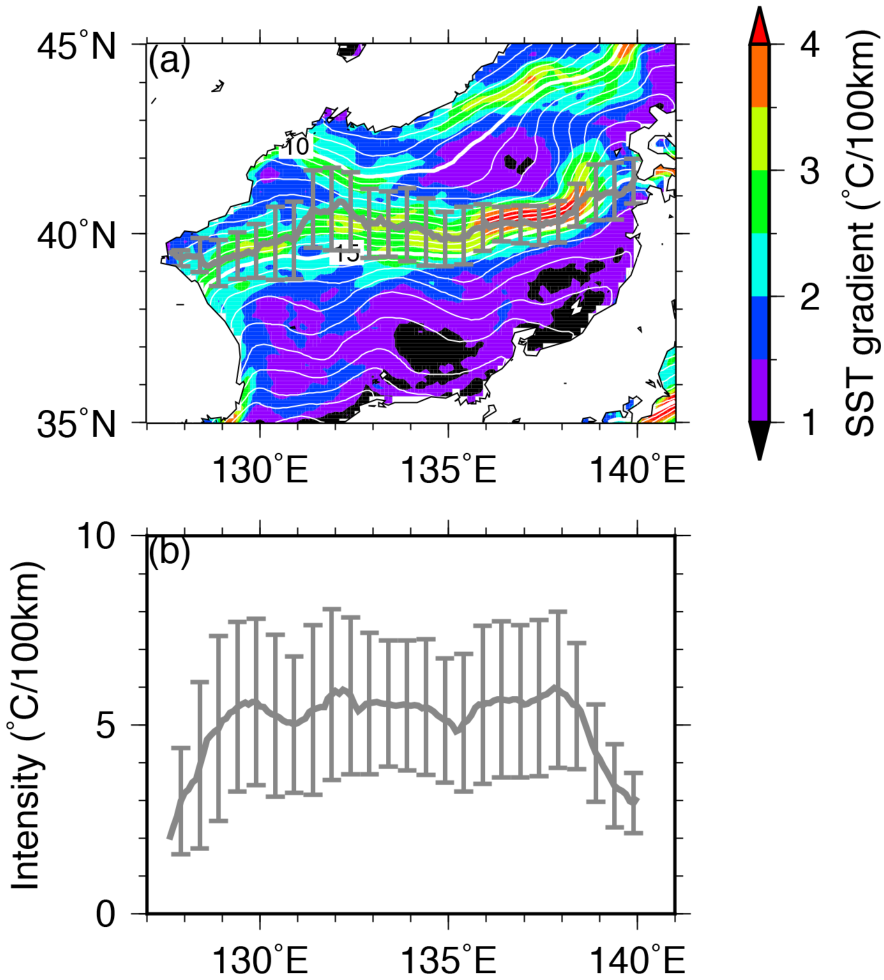

Fig. 2 Annual mean of the (a) position and (b) intensity of the SST front. Error bars are standard deviations in the analysis period. In (a), color indicates the amplitude of the SST gradient and white contour denotes SST climatology. Thin (Thick) contour intervals are 0.5 (5) °C.

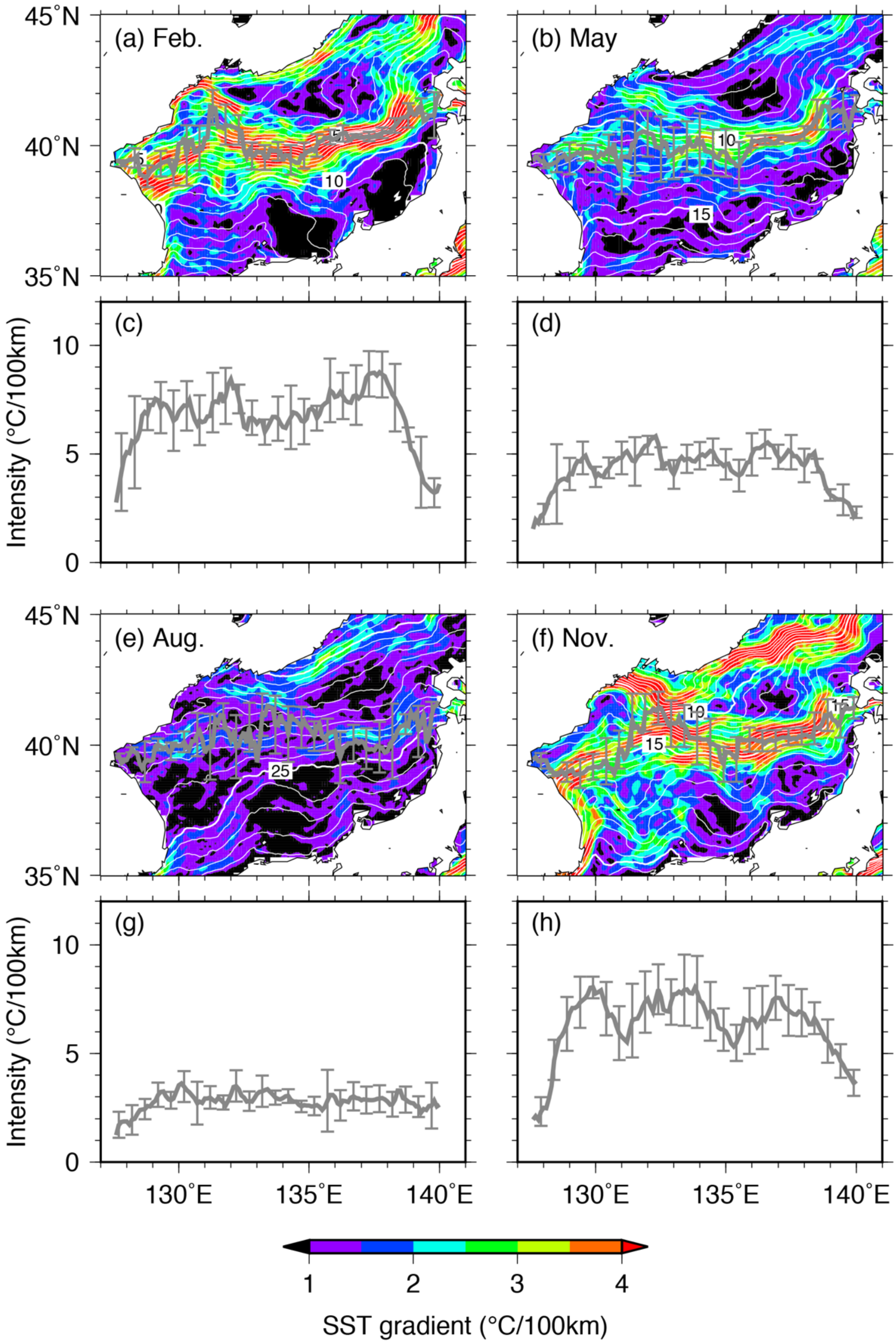

Fig. 3 As in Fig. 2, but for monthly mean in (a), (c) February, (b), (d) May, (e), (g) August, and (f), (h) November.

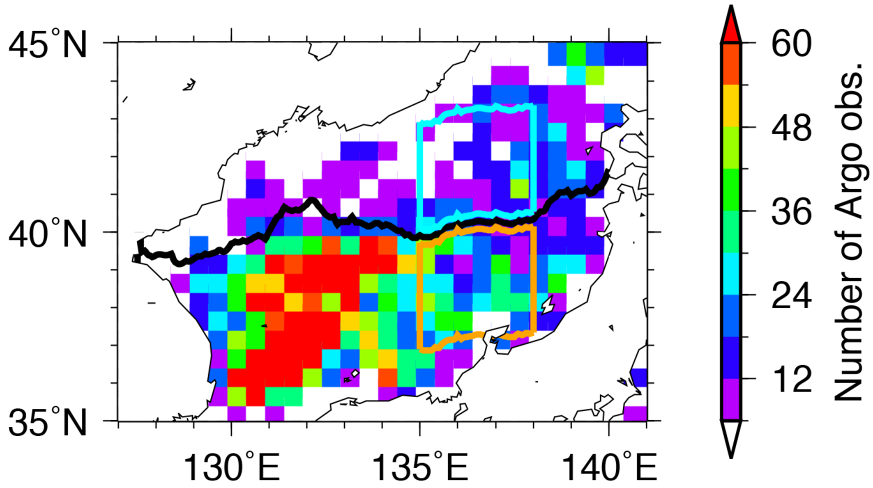

Fig. 4 The total number of observations by the Argo floats in 2007–2011. A black line shows the annual mean of the SST front position. An orange (A cyan) box denotes the 3° longitude × 3° latitude averaging area on the southern (northern) side of the SST front. Note that white color indicates less than 6 observations.

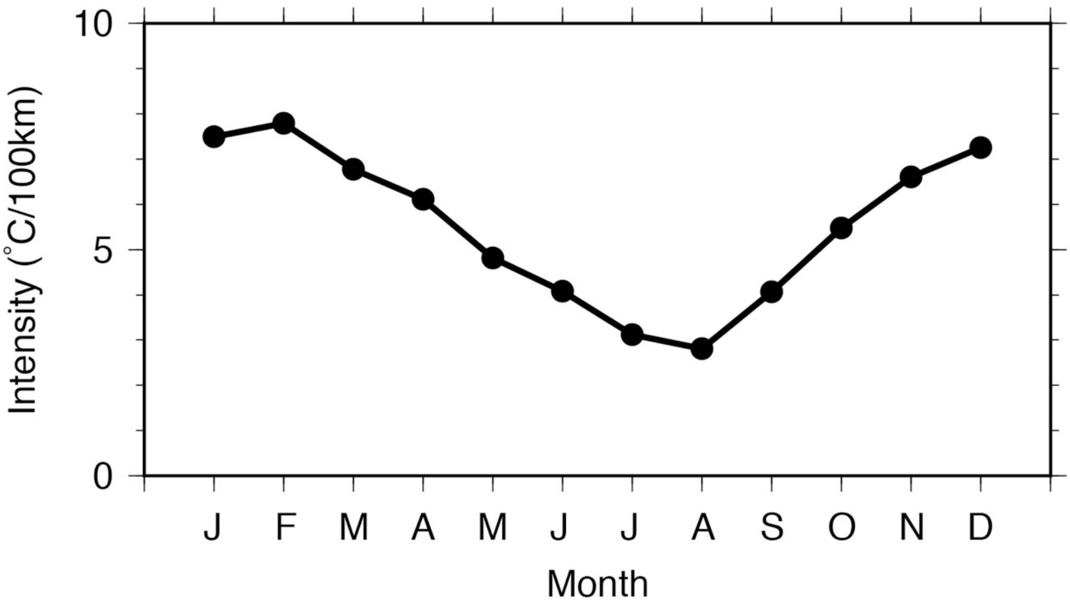

Fig. 5 Monthly-mean intensity of the SST front averaged within 135°–138°E, which is derived from MURSST.

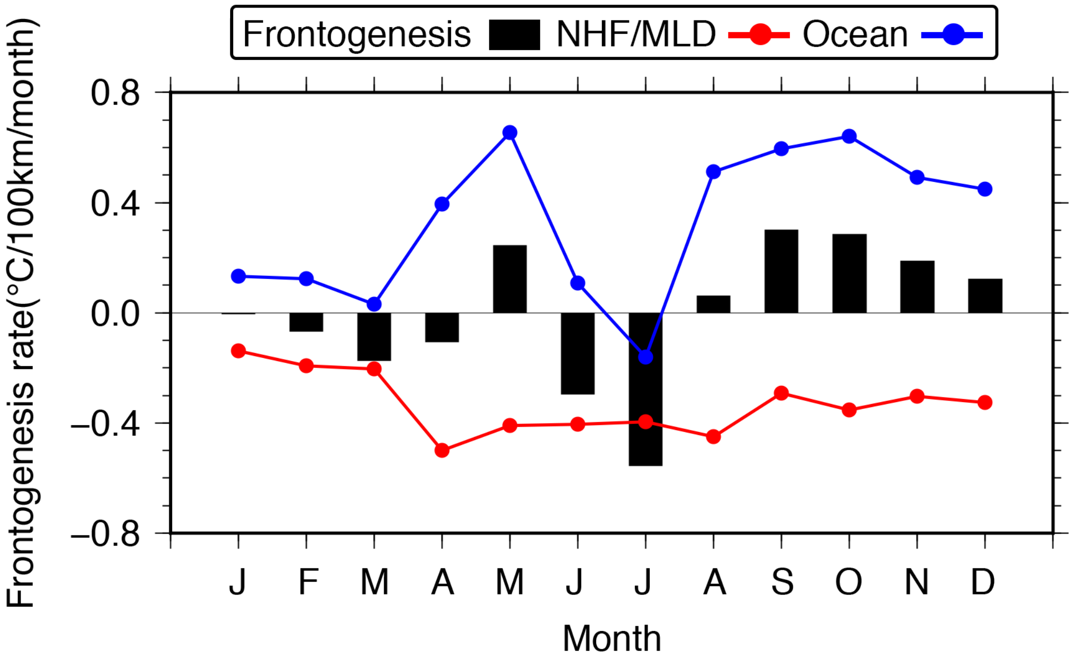

Fig. 6 Monthly climatology of each term of Eq. (1): the frontogenesis rate [the left-hand side term (LHS); black bar] estimated from MIMOC, the surface net heat flux (NHF)/MLD gradient term [the 1st term on the right-hand side (RHS); red line], and the oceanic term gradient (the 2nd term on the RHS; blue line).

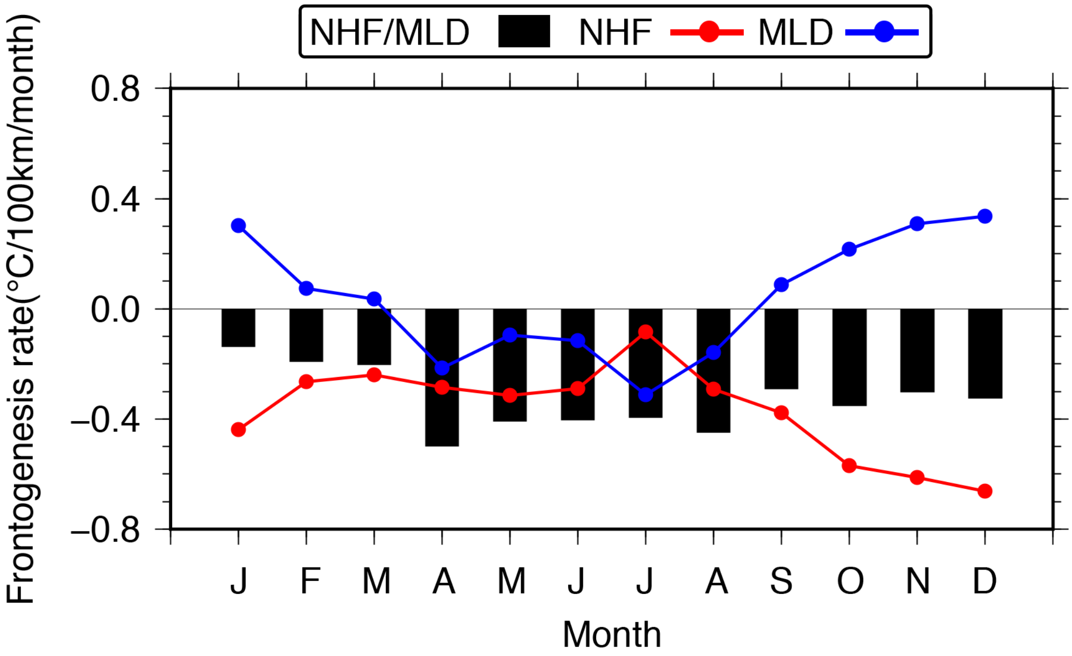

Fig. 7 Monthly climatology of each term of Eq. (3): the NHF/MLD gradient term (the LHS term; black bar), the NHF gradient term (the 1st term on the RHS; red line), and the MLD gradient term (the 2nd term on the RHS; blue line).

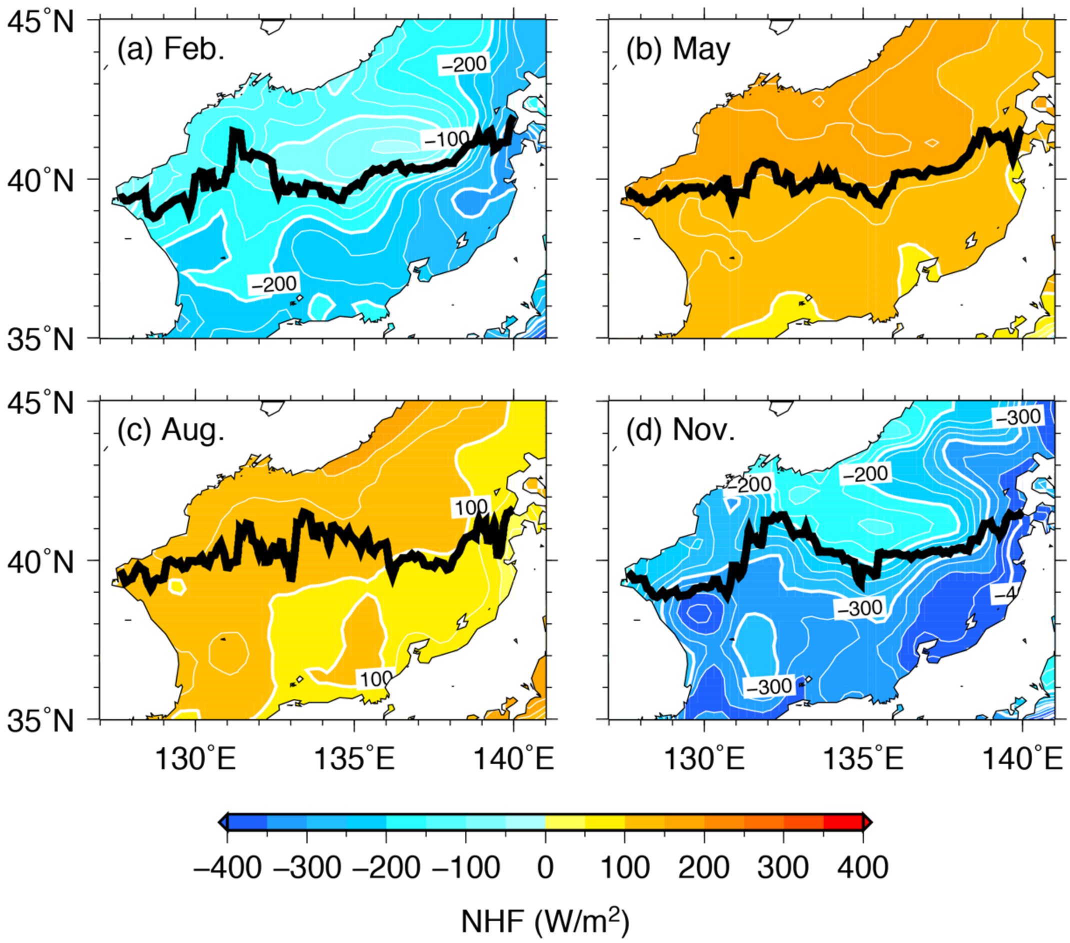

Fig. 8 Monthly climatology of NHF in (a) February, (b) May, (c) August, and (d) November. Thin (Thick) counter intervals are 25 (100) W/m2.

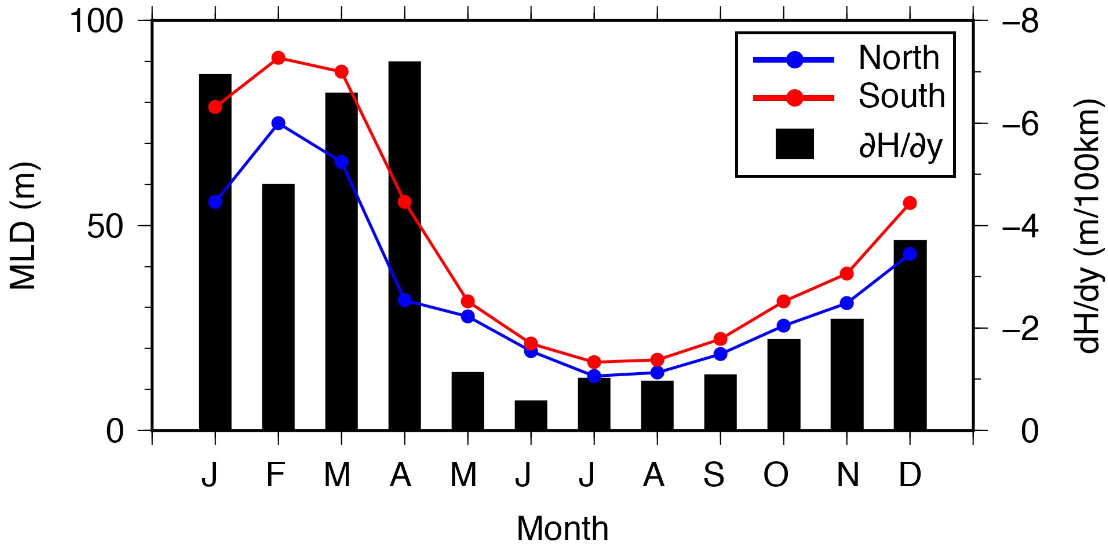

Fig. 9 Monthly climatology of the MLD on the southern (red line) and northern (blue line) sides of the front and the MLD gradient (black bar).

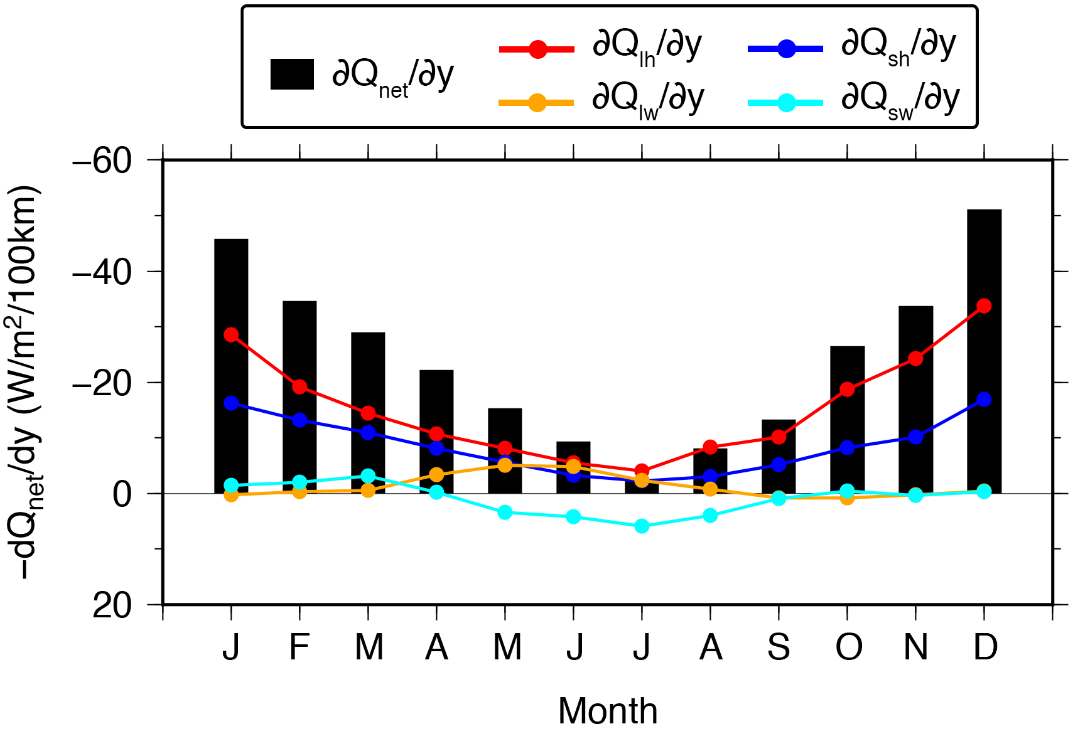

Fig. 10 Monthly climatology of each term of Eq. (4): the NHF gradient (the LHS term; black bar), the latent/sensible flux gradient term (the 1st/2nd term on the RHS; red/blue line), and the longwave/shortwave radiation gradient term (the 3rd/4th term on the RHS; orange/cyan line).

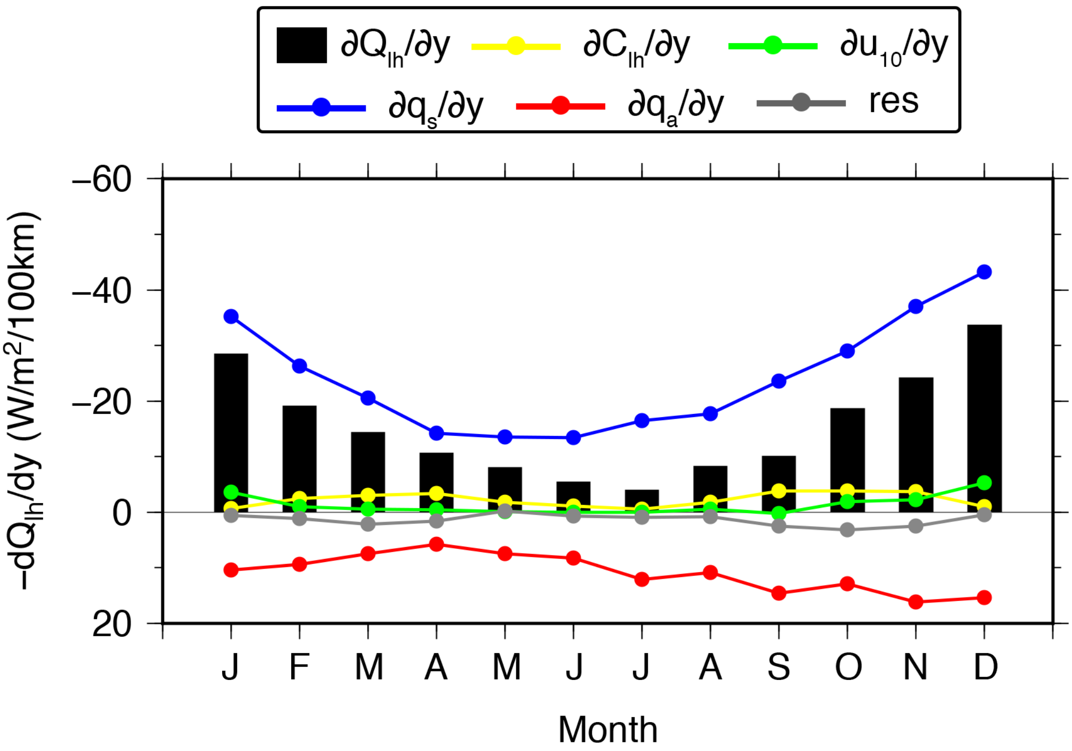

Fig. 11 Monthly climatology of each term of Eq. (5): the latent heat flux gradient (the LHS term), the latent heat coefficient gradient term (the 1st term on the RHS; yellow line), the wind speed gradient term (the 2nd term on the RHS; green line), the surface saturated specific humidity gradient term (the 3rd term on the RHS; blue line), the air specific humidity gradient term (the 4th term on the RHS; red line), and the residual term (the last term on the RHS; gray line).

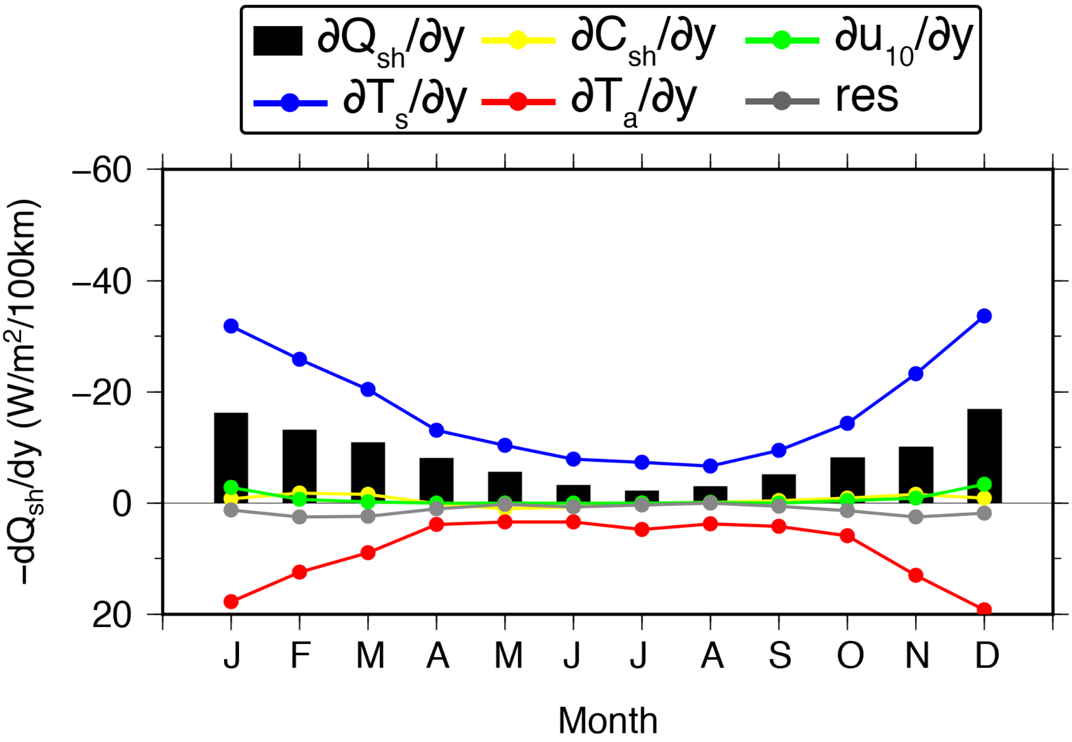

Fig. 12 Monthly climatology of each term of Eq. (6): the sensible heat flux gradient (the LHS term; black bar), the sensible heat coefficient gradient term (the 1st term on the RHS; yellow line), the wind speed gradient term (the 2nd term on the RHS; green line), the SST gradient term (the 3rd term on the RHS; blue line), the air temperature gradient term (the 4th term on the RHS; red line), and the residual term (the last term on the RHS; gray line).

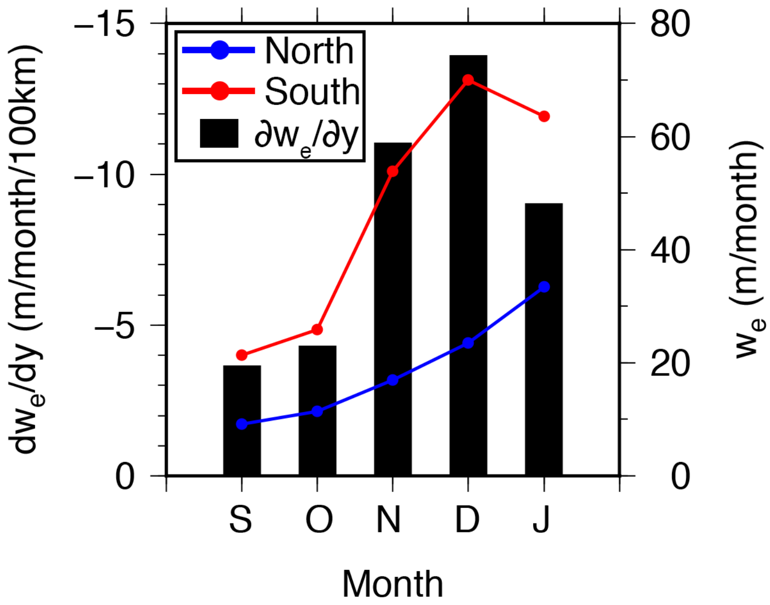

Fig. 13 Monthly climatology of the diagnostic entrainment velocity gradient (black bar), and the entrainment velocity on the southern (red line) and northern (blue line) sides in September–January when the observed MLD deepens on the both sides of the front.

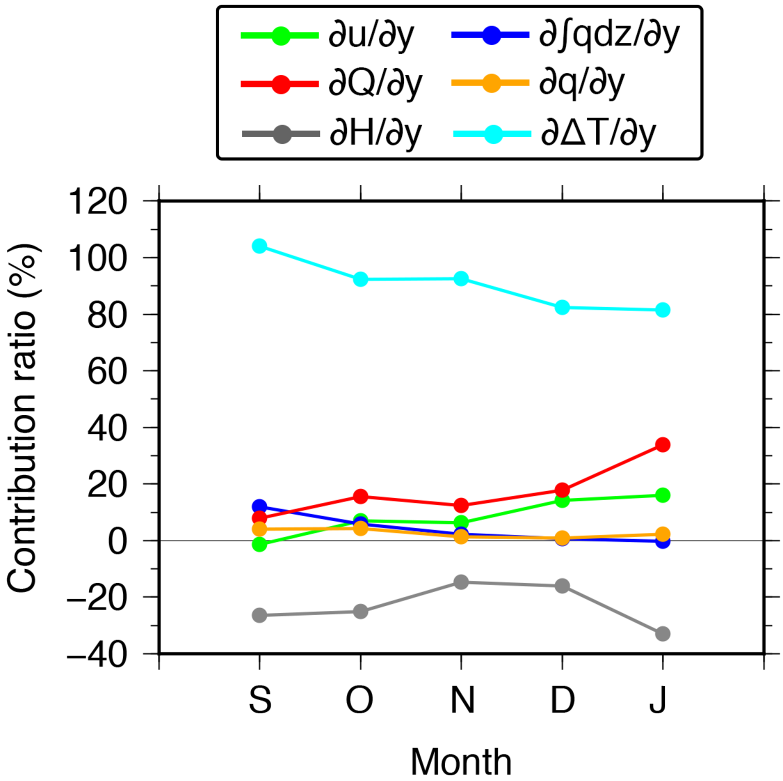

Fig. 14 Monthly climatology of contribution ratios of each term on the RHS of Eq. (8) to the diagnostic entrainment velocity gradient [the LHS term of Eq. (8)]: the gradients of the wind speed (the 1st term; green), incidence of shortwave radiation (the 2nd term; blue), NHF (the 3rd term; red), downward shortwave radiation at the base of mixed layer (the 4th term; orange), MLD (the 5th term; gray), and stratification (the last term; cyan).

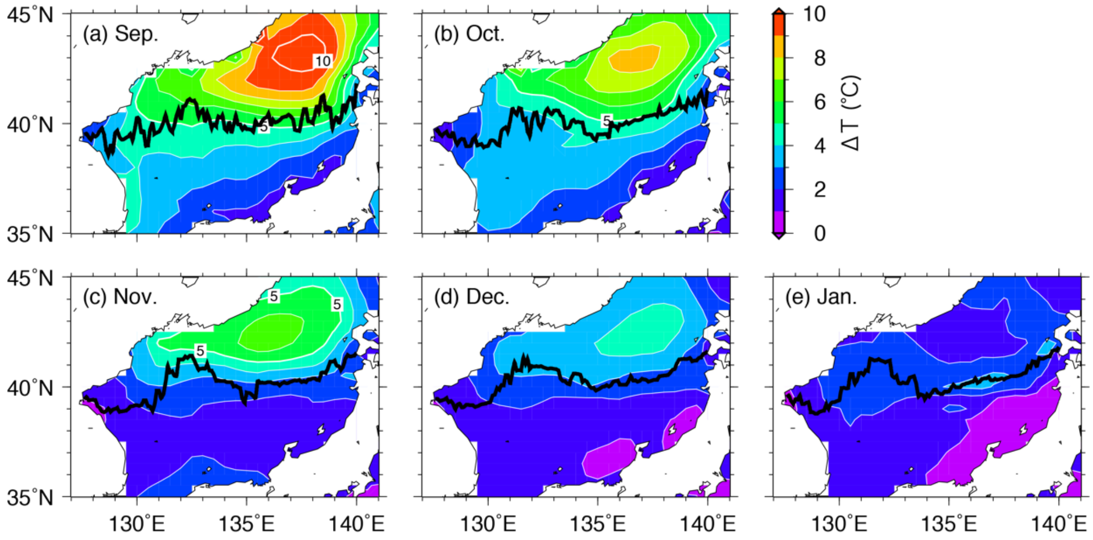

Fig. 15 Monthly climatology of the temperature difference between the mixed layer and entrained water in September–January. Black line denotes the monthly climatological SST front position. Thin (Thick) white contour intervals are 1 (5) °C.

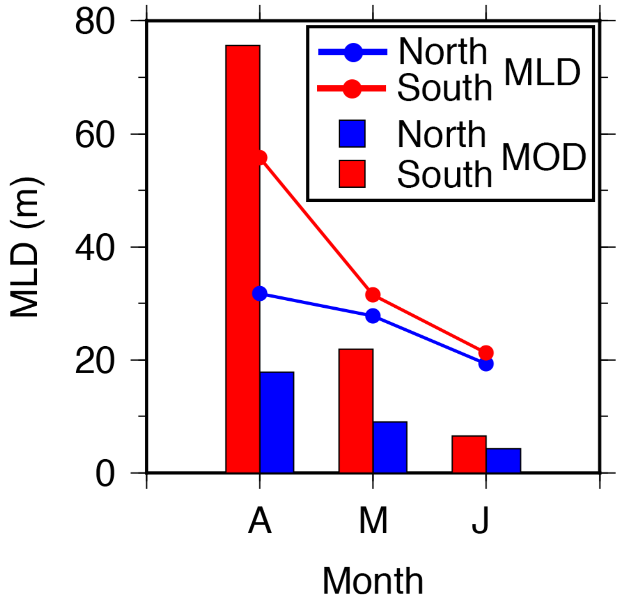

Fig. 16 Monthly climatology of the Monin-Obukhov Depth (MOD; bar) and observed MLD (line) on the southern (red) and northern (blue) regions in April–June when the MLD becomes shallower on both sides of the front.

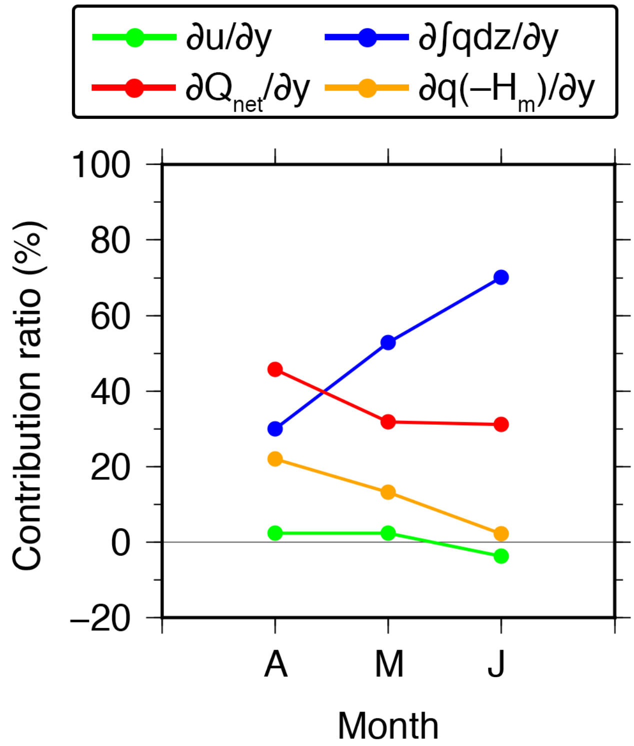

Fig. 17 Monthly climatology of contribution ratios from each term on the RHS of Eq. (10) to the MOD gradient [the LHS term of Eq. (10)]: the gradients of the wind speed (the 1st term; green), incidence of shortwave radiation (the 2nd term; blue), NHF (the 3rd term; red), and shortwave radiation at the base of the MOD (the 4th term; orange) in April–June.

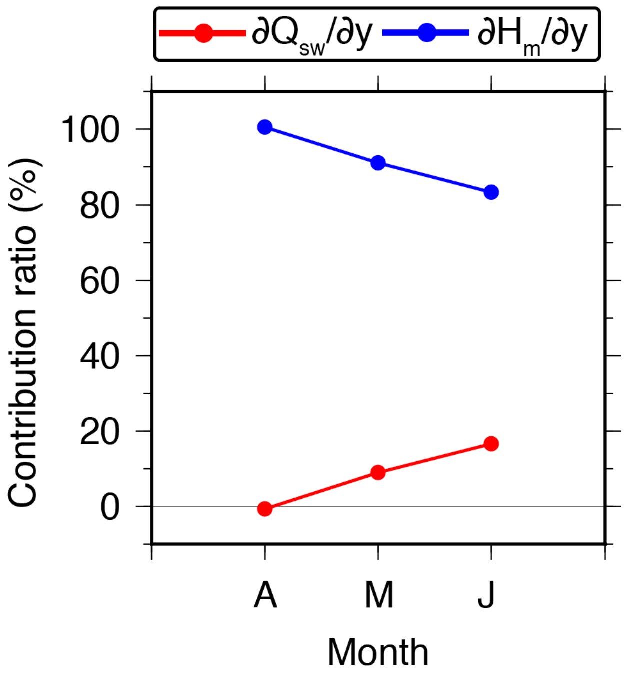

Fig. 18 Monthly climatology of contribution ratios from the gradients of shortwave radiation [the 1st term on the RHS of Eq. (11); red] and MOD [the 2nd term on the RHS of Eq. (11); blue] to the shortwave radiation incidence gradient [the LHS term of Eq. (11)] in April–June.

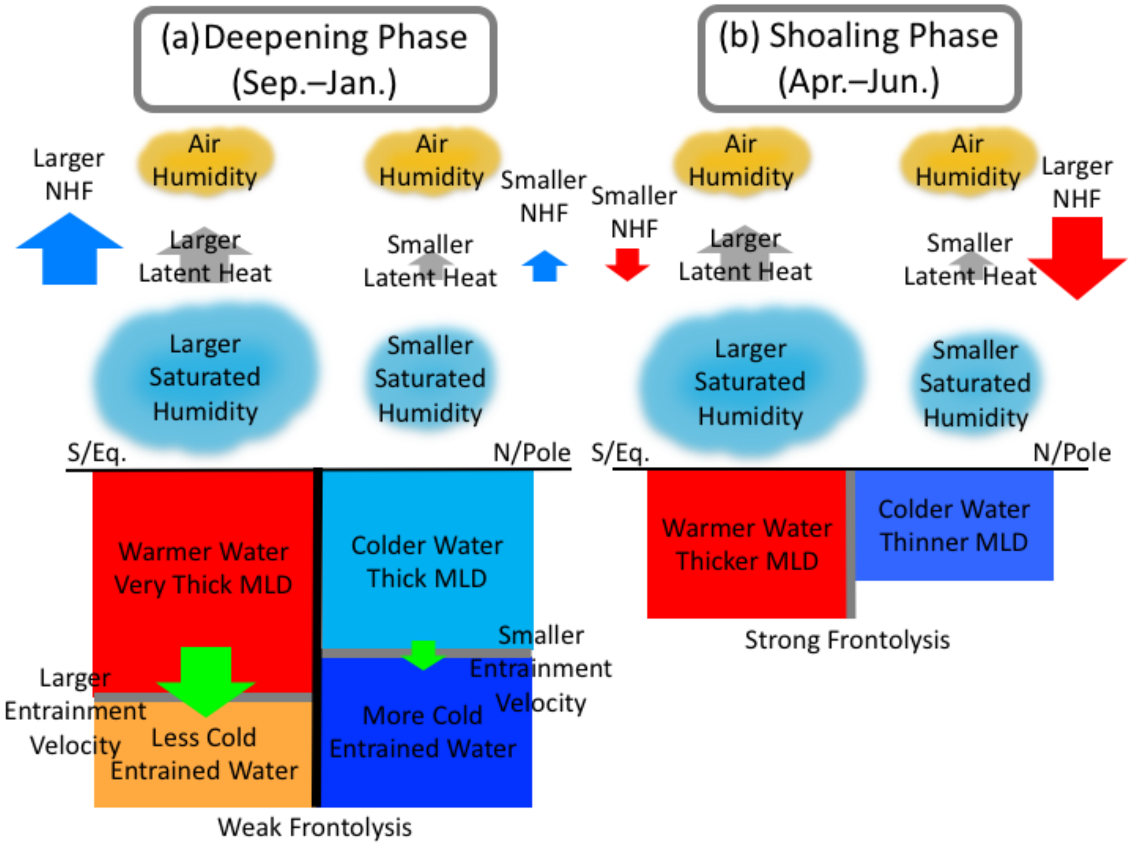

Fig. 19 Schematic diagrams of frontolysis by surface heat flux in the eastern Japan Sea during the (a) deepening and (b) shoaling phase.